Радиофизика и радиоастрономия. 2015, Т. 20, № 2, с. 154–167

РАДИОФИЗИЧЕСКИЕ АСПЕКТЫ РАДИОЛОКАЦИИ, РАДИОНАВИГАЦИИ, СВЯЗИ И ДИСТАНЦИОННОГО ЗОНДИРОВАНИЯ

O. O. BEZVESILNIY, D. M. VAVRIV, V. A. VOLKOV, A. A. KRAVTSOV, E. V. BULAKH, V. V. VINOGRADOV, AND S. S. SEKRETAROV

Institute of Radio Astronomy, National Academy of Sciences of Ukraine, 4, Chervonopraporna St., Kharkiv, 61002, Ukraine
E-mail: vavriv@rian.kharkov.ua, obezv@rian.kharkov.ua

EXPERIMENTAL KA-BAND GROUND-BASED SAR SYSTEM

An experimental ground-based synthetic aperture radar (GB-SAR) system operating at Ka-band has been developed. The system is designed to be operated from a top a hill or from a building roof, etc. for imaging the underlying ground terrain. The radar hardware system, operating mode and original data processing techniques are described in the paper. A high-duty-cycle long-LFM-pulse mode (quasi-continuous mode) has been used. An effective adaptive matched filtering for range compression has been introduced that provides high dynamic range and high coherency for the radar system. A prominent point processing autofocus has been implemented for the precise estimation and compensation of motion errors of the radar platform. The achieved performance of the GB-SAR system is illustrated with experimental data.

Keywords: synthetic aperture radar (SAR), ground-based SAR, pulse compression side lobes, motion error compensation, autofocusing, radar applications, radar remote sensing

1. Introduction

Ground-based synthetic aperture radar (GB-SAR) systems are placed a top a hill or on a building roof, etc. and used for imaging of the underlying ground terrain with high spatial resolution. The GB-SAR systems are used for a variety of applications [1–6], for example, for monitoring changes in the environment, for observation of open-air mining sites, for ships safety monitoring in ports, for surveillance of runways in airports, and so on.

The GB-SAR imaging geometry is illustrated in Fig. 1. The GB-SAR antenna typically has a rather wide beam (for example, 40°) in the horizontal plane (in the azimuth) and a moderately wide beam (for example, 15°) in the vertical plane (in the elevation). With such an antenna, the radar illuminates a wide sector of the scene.

The high range resolution is achieved due to the pulse compression technique. Typically, the pulses with linear frequency modulation (LFM) are used providing the range resolution

$$\rho_R = K_R c/(2B_{\mathrm{LFM}}), \qquad (1)$$

where B_{LFM} is the LFM pulse frequency bandwidth, K_R is the broadening coefficient that comes from the weighting window applied to control the compression side lobes, c is the speed of light.

The high azimuth resolution is provided by the synthetic aperture technique. The radar is placed on a moving platform that is translated in a direction across the radar beam (see Fig. 1). The backscattered radar pulses are collected along the path and combined coherently to form the synthetic aperture. The platform path length is the length of the synthetic aperture. The GB-SAR platform is typically a kind of a trolley on rails, and the aperture length is commonly limited to a few meters, thus limiting the azimuth resolution. The aperture length is constant for all

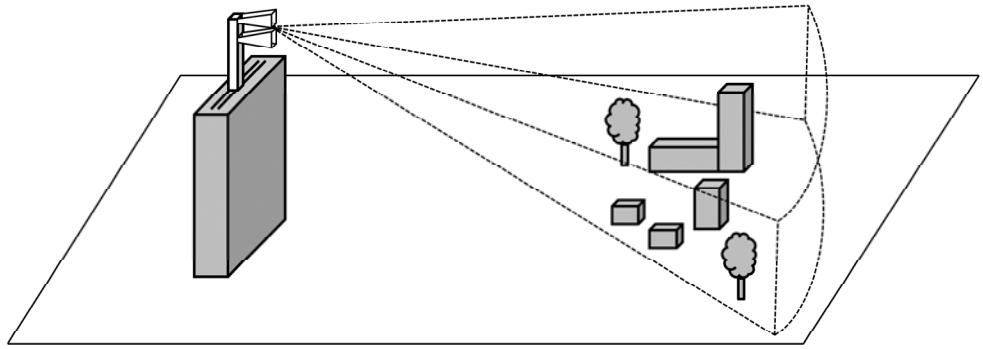

Fig. 1. GB-SAR imaging geometry

ranges. As a result, the azimuth resolution of GB-SAR systems is range-dependent; actually, the azimuth resolution is the angular resolution determined as

$$\theta_X = \frac{\rho_X}{R} = K_X \frac{\lambda}{2L_S}, \qquad (2)$$

where ρ_X is the cross-range resolution in meters at range R, K_X being the broadening coefficient of the weighting window applied in the azimuth direction, λ is the radar wavelength, and L_S is the synthetic aperture length. In contrast to the GB-SAR, for the airborne or satellite SAR, there is a possibility to enlarge the synthetic aperture length (the length of the flight trajectory) proportionally to the range R in order to keep the azimuth resolution ρ_X constant.

An important peculiarity of the GB-SAR system is that it should operate from very close ranges to a few kilometers. Otherwise speaking, the radar should receive the backscattered signal from the very start of the pulse transmission. It means that the radar should transmit and receive signals simultaneously. With the simultaneous transmission and reception, the receiver faces the problem of the strong input signal that is a sum of the part of the transmitter signal leaking within the radar hardware and the strong signal reflected from very close targets surrounding the radar. This undesired strong input signal limits the radar ability to detect useful weak signals from far targets. One of the possibilities to solve the problem is usage of two separate antennas for transmission and reception. Such an approach allows reducing the transmitter signal leakage at the receiver input to the level better than about –50 dB. However, such an approach does not solve the problem of a strong signal from nearby targets. Thus, the receiver with high dynamic range is still required. Another problem with the strong input signal is related to the pulse compression side lobes. The side lobes from close targets could be higher than the useful signals from far targets. Thus, some additional efforts are required to obtain very low pulse compression side lobes.

In order to solve the aforesaid problems, an effective adaptive matched filtering for range compression has been introduced that provides high dynamic range and high coherency for the radar system. A two-channel receiver is used to record both the transmitted pulse and the backscattered pulse. The matched filter is adjusted to each transmitted pulse, compensating possible imperfections of the transmitted LFM waveforms to obtain good pulse compression side lobes. Also, such an approach improves the pulse-to-pulse radar coherency as a bonus. Apparently, this approach reduces the requirements to the radar hardware system, in particular, to the accuracy of the generated LFM waveforms.

The adaptive matched filter approach poses the following restriction on the radar pulse operation mode. Two consequent transmitted pulses should not overlap in the backscattered signal. Therefore, a long-LFM-pulse mode with a high duty cycle (a kind of quasi-continuous mode) has been implemented.

Usually, the GB-SAR platform is well stabilized and its translational motion provided by a step-motor is uniform. However, a firm ground platform is usually quite heavy. In our experimental GB-SAR system, we used a fairly light platform and did not pay much attention to its stabilization and uniformity of motion. Such an approach could be more appropriate for a light-weight mobile GB-SAR sys-

tem exploited in the field conditions. Instead, we have developed an effective autofocus approach for post-processing of the recorded data. The well-known prominent point processing autofocus technique [7, 8] has been specially adapted to measure the ground platform motion errors. During the SAR image formation, the estimated motion errors can be compensated.

The described approaches have been implemented and tested in the experimental Ka-band GB-SAR system developed at the Institute of Radio Astronomy of the National Academy of Sciences of Ukraine. The radar hardware is described in Section 2. The adaptive matched filter design is discussed in Section 3. The long-LFM-pulse operating mode is considered in Section 4. The GB-SAR data processing steps are described in Section 5. The proposed autofocus technique is described in Section 6. The obtained results are demonstrated and discussed in Section 7.

2. Radar Hardware System

Main characteristics of the GB-SAR system are listed in Table 1. A simplified block diagram of the GB-SAR hardware system is shown in Fig. 2. The transmitter is built on two heterodynes and a direct digital frequency synthesizer (DDS). The 1st heterodyne is based on a dielectric resonator and generates the signal at frequency of 8.5 GHz. The 2nd heterodyne uses a voltage-controlled oscillator (VCO) and generates the signal at frequency of 1380 MHz.

Table 1. **Characteristics of the GB-SAR system**

Radar frequency	35 GHz
Transmitted power	< 1 W
Pulse repetition frequency	2.5 kHz
Pulse duration	250 μs
Duty cycle	62.5 %
3-dB antenna beam width in horizontal/vertical plane	40°/10°
LFM pulse bandwidth	48 MHz
Range resolution	4 m
Length of the synthetic aperture	~ 1 m
Trolley motion time/speed	~ 5 s / 20 cm · s^{-1}
Synthetic beam width (angular resolution)	0.32°
Cross-range resolution (it grows linearly with range)	~ 1 m at 200 m range

The signal with LFM at the carrier frequency of 280 MHz is formed with the DDS. The synchronization is performed with a 100-MHz reference signal from a crystal oscillator. The signals from the DDS and the 2nd heterodyne come to a quadrature modulator which is used to form the LFM signal at the carrier frequency of 1100 MHz. The obtained signal and the signal from the 1st heterodyne (multiplied by 4) come to a mixer and a power amplifier which finally forms the transmitter signal at 35.1 GHz. The power of the transmitter signal which feeds the transmitting antenna is about 1 W. A small part of the transmitter signal (about –50 dB) is split here to the 2nd channel

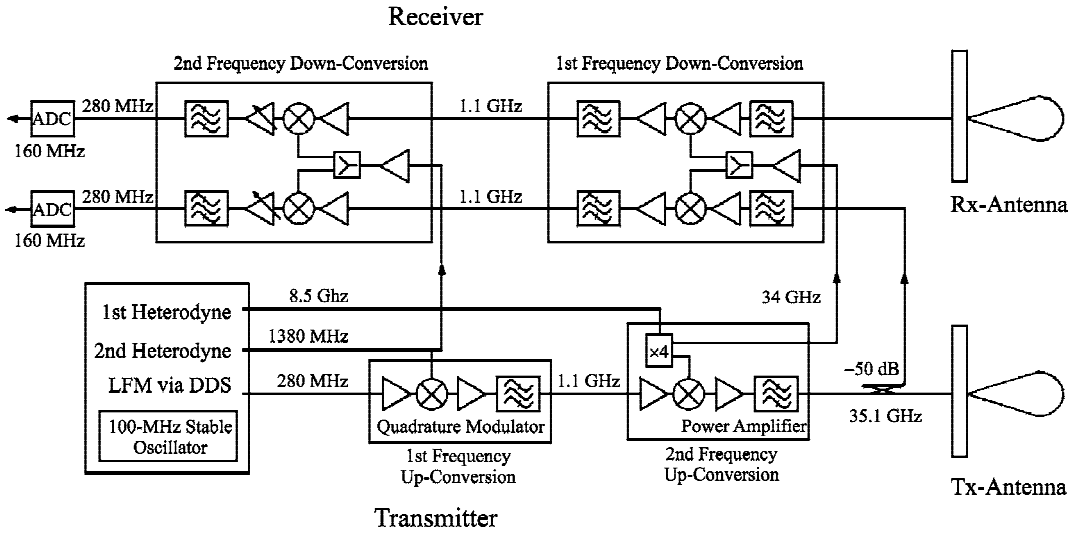

Fig. 2. GB-SAR hardware system

of the receiver. It is required for the adaptive pulse compression.

The receiver has two identical channels [9]. The 1st one is used to sample the backscattered pulses, and the 2nd one is required to sample the transmitted pulses. The received signals are amplified, filtered and transformed consequently to the 1st intermediate frequency of 1100 MHz and then to the 2nd intermediate frequency of 280 MHz. The obtained signals are sampled with two 16-bits ADCs at 160 MHz and, finally, come to a digital signal processing system for further processing, including the digital quadrature demodulation, range compression, etc.

The system has two separate horn antennas for simultaneous transmission of long LFM pulses and reception of radar returns. The antennas beam width is $40°$ in the horizontal plane and $10°$ in the vertical one.

During our experiments, the GB-SAR system has been set up on a trolley on rails as is shown in Fig. 3. The received radar data are recorded on a hard disk drive on a common PC that has also been placed on the trolley.

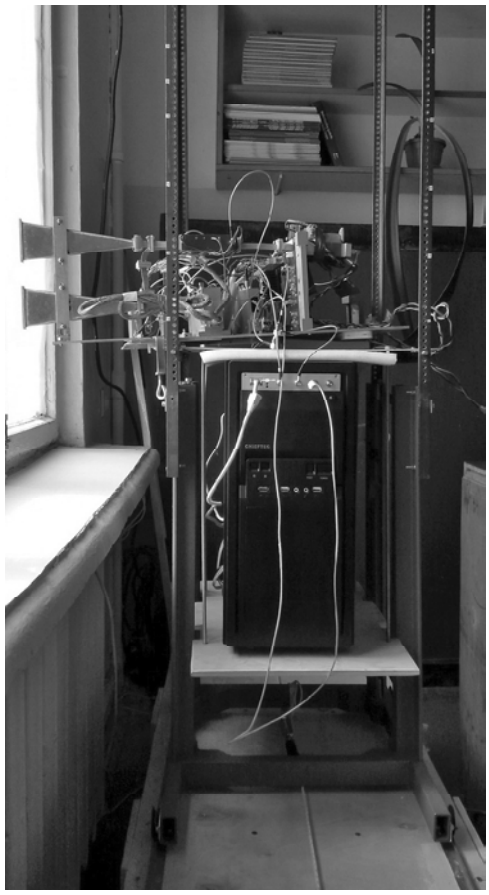

Fig. 3. GB-SAR system setup on a trolley on rails

3. Adaptive Pulse Compression Technique

The radar transmitter forms the long LFM Tx-pulses of duration τ_{LFM} that can be written as

$$p_{\text{Tx}}(n, \tau) = w_{\text{Tx}}(n, \tau)\, p_{\text{LFM}}(\tau) \exp\left[i\varphi_{\text{Tx}}(n, \tau)\right], \quad (3)$$
$$0 \le \tau \le \tau_{\text{LFM}}.$$

Here n is the pulse number, τ is the fast time (in the range direction), $w_{\text{Tx}}(n, \tau)$ is the Tx-pulse envelope, and $\varphi_{\text{Tx}}(n, \tau)$ is the Tx-pulse phase noise as compared to the reference LFM waveform

$$p_{\text{LFM}}(\tau) = \exp\left[i\pi\gamma_{\text{LFM}}(\tau - \tau_{\text{LFM}}/2)^2\right], \quad (4)$$

γ_{LFM} is the LFM rate. Note that the pulse envelope $w_{\text{Tx}}(n, \tau)$ and pulse phase noise $\varphi_{\text{Tx}}(n, \tau)$ may vary from pulse to pulse as indicated by the pulse number n. In this way, the model accounts for the imperfection of the generated LFM pulses as well as for possible deviations of radar coherency. The Tx-pulses (3) are recorded via the 2nd channel of the receiver.

The radar echo signal is a sum of the LFM Rx-pulses $p_{\text{Rx}}(n, \tau)$ backscattered from the targets located within the antenna beam:

$$s_{\text{Rx}}(n, \tau) = \sum_m a_m \exp\left[-i(4\pi/\lambda)R_m\right] p_{\text{Rx}}(n, \tau - \tau_m), \quad (5)$$
$$\tau_m = 2R_m/c, \quad 0 \le \tau \le \tau_{\text{LFM}} + 2R_{\max}/c.$$

The amplitudes a_m are determined by the radar cross sections of the targets, and the delays $\tau_m = 2R_m/c$ are related to the ranges R_m to the targets, c is the speed of light, $R_{\max}$ is the maximum range. The Rx-pulses can be written as

$$p_{\text{Rx}}(n, \tau) = w_{\text{Rx}}(n, \tau)\, p_{\text{LFM}}(\tau) \exp[i\varphi_{\text{Rx}}(n, \tau)], \quad (6)$$
$$0 \le \tau \le \tau_{\text{LFM}}.$$

The received signal (5) is recorded via the 1st channel of the receiver.

The envelope $w_{\text{Rx}}(n, \tau)$ and the phase distortions $\varphi_{\text{Rx}}(n, \tau)$ of the Rx-pulses (6) could be different from those of the Tx-pulses (3). This difference comes from the fact that the Rx-pulses (6) go through the different hardware chains than the Tx-pulses (3). In particular, the Tx-pulses do not go through the transmitting and receiving antennas in contrast to the Rx-pulses. The Tx-pulses and Rx-pulses can be related to each other in the frequency domain via the transfer function:

$$H_{\mathrm{Tx/Rx}}(f)=\frac{P_{\mathrm{Tx}}(n,\,f)}{P_{\mathrm{Rx}}(n,\,f)},\qquad(7)$$

where $P_{\mathrm{Tx}}(n,\,f)$ and $P_{\mathrm{Rx}}(n,\,f)$ are the Fourier spectra of the Tx-pulse and Rx-pulse, respectively. The transfer function is assumed to be independent on the pulse number; it may be estimated by analyzing the signals backscattered from bright isolated point scatterers.

The LFM pulse compression is typically performed as a convolution of the received radar signal $s_{\mathrm{Rx}}(n,\,\tau)$ with the mathematical reference LFM pulse:

$$p_{\mathrm{ref}}(\tau)=w_{\mathrm{ref}}(\tau)\,p_{\mathrm{LFM}}(\tau).\qquad(8)$$

Here $w_{\mathrm{ref}}(\tau)$ is the weighting window of the length of τ_{LFM} applied to control the compression side lobes. The convolution can be calculated either in the time domain as

$$s_{\mathrm{RC}}(n,\tau)=\int_0^{\tau_{\mathrm{LFM}}} s_{\mathrm{Rx}}(n,\,\tau+\tau')\,p^{*}_{\mathrm{ref}}(\tau')\mathrm{d}\tau',\qquad(9)$$

$$0\le\tau\le 2R_{\max}/c,$$

or in the frequency domain as

$$s_{\mathrm{RC}}(n,\,\tau)=\frac{1}{2\pi}\int_{-B_{\mathrm{LFM}}/2}^{B_{\mathrm{LFM}}/2} S_{\mathrm{Rx}}(n,\,f)\,P^{*}_{\mathrm{ref}}(f)\exp[2\pi i f\tau]\mathrm{d}f.\qquad(10)$$

Here $s_{\mathrm{RC}}(n,\,\tau)$ is the range-compressed signal, $S_{\mathrm{Rx}}(n,\,f)$ and $P_{\mathrm{ref}}(f)$ are the Fourier spectra of the Rx-signal (6) and the reference LFM pulse (8), respectively, and

$$B_{\mathrm{LFM}}=\gamma_{\mathrm{LFM}}\tau_{\mathrm{LFM}}\qquad(11)$$

is the LFM pulse frequency bandwidth. In practice, the computations are commonly performed in the frequency domain as (10) by using the fast Fourier transform (FFT).

Accounting that the Rx-signal is the sum of the backscattered pulses (5) one can easily derive the following expression for the spectrum of the Rx-signal:

$$S_{\mathrm{Rx}}(n,\,f)=$$
$$=\sum_m a_m\exp\left[-i(4\pi/\lambda)R_m\right]P_{\mathrm{Rx}}(n,\,f)\exp[-2\pi i f\tau_m].\qquad(12)$$

By substituting expression (12) into (10), one can write the range-compressed signal as a sum

$$s_{\mathrm{RC}}(n,\,\tau)=\sum_m a_m\exp\left[-i(4\pi/\lambda)R_m\right]p_{\mathrm{RC}}(\tau-\tau_m),\qquad(13)$$

of the short range-compressed pulses

$$p_{\mathrm{RC}}(n,\,\tau)=$$
$$=\frac{1}{2\pi}\int_{-B_{\mathrm{LFM}}/2}^{B_{\mathrm{LFM}}/2} P_{\mathrm{Rx}}(n,\,f)\,P^{*}_{\mathrm{ref}}(f)\exp[2\pi i f\tau]\mathrm{d}f.\qquad(14)$$

The short compressed pulse $p_{\mathrm{RC}}(n,\,\tau)$ differs from the physical short radar pulse by the presence of compression side lobes. Application of the weighting window $w_{\mathrm{ref}}(\tau)$ in the reference LFM pulse (8) along with the appropriate pulse envelopes $w_{\mathrm{Tx}}(n,\,\tau)$ in the Tx-pulse (3) and $w_{\mathrm{Rx}}(n,\,\tau)$ in the Rx-pulse (6) allows reducing the side lobes to a desired low level. However, when the extremely low side lobes are required, the phase noise and other distortions presented in the actually transmitted LFM waveform result in growing of the side lobes despite of the applied weighting windows. In order to achieve extremely low side lobes, the matched filter should be specially designed to account for the imperfections of the transmitted waveforms.

The idea of the adaptive range compression filter lies in compensation of the actual Rx-pulse spectrum $P_{\mathrm{Rx}}(n,\,f)$ under the integral (14) to the reference Rx-pulse spectrum $P_{\mathrm{Rx\,ref}}(f)$:

$$p_{\mathrm{RC\,Adapt}}(\tau)=\frac{1}{2\pi}\int_{-B_{\mathrm{LFM}}/2}^{B_{\mathrm{LFM}}/2} P_{\mathrm{Rx\,ref}}(f)\,P^{*}_{\mathrm{ref}}(f)\exp[2\pi i f\tau]\mathrm{d}f.\qquad(15)$$

The reference Rx-pulse $p_{\mathrm{Rx\,ref}}(\tau)$ and its spectrum $P_{\mathrm{Rx\,ref}}(f)$ are similar to the reference LFM pulse (8) except for the weighting window $w_{\mathrm{Rx\,ref}}(\tau)$ which can be selected separately to balance the compression side lobes and the resolution:

$$p_{\mathrm{Rx\,ref}}(\tau)=w_{\mathrm{Rx\,ref}}(\tau)\,p_{\mathrm{LFM}}(\tau).\qquad(16)$$

Thus, the actual spectrum $P_{\mathrm{Rx}}(n,\,f)$ under the integral (14) should be multiplied by some compensation function $R_{\mathrm{Comp}}(n,\,f)$ to obtain the desired reference spectrum $P_{\mathrm{Rx\,ref}}(f)$ (15):

$$P_{\mathrm{Rx}}(n,\,f)R_{\mathrm{Comp}}(n,\,f)=P_{\mathrm{Rx\,ref}}(f). \tag{17}$$

From this equation, using the transfer function (7), the compensation function can be found as

$$R_{\mathrm{Comp}}(n,\,f)=\frac{P_{\mathrm{Rx\,ref}}(f)}{P_{\mathrm{Rx}}(n,f)}=\frac{P_{\mathrm{Rx\,ref}}(f)}{P_{\mathrm{Tx}}(n,f)}H_{\mathrm{Tx/Rx}}(f). \tag{18}$$

For the adaptive range compression of the received signal, this compensation function should be applied under the integral (10) as

$$s_{\mathrm{RC\,Adapt}}(n,\tau)=$$

$$=\frac{1}{2\pi}\int_{-B_{\mathrm{LFM}}/2}^{B_{\mathrm{LFM}}/2}S_{\mathrm{Rx}}(n,\,f)R_{\mathrm{Comp}}(n,f)P^{*}_{\mathrm{ref}}(f)\exp[2\pi if\tau]\mathrm{d}f. \tag{19}$$

Finally, the adaptive matched filter can be written as

$$s_{\mathrm{RC\,Adapt}}(n,\,\tau)=$$

$$=\frac{1}{2\pi}\int_{-B_{\mathrm{LFM}}/2}^{B_{\mathrm{LFM}}/2}S_{\mathrm{Rx}}(n,\,f)P^{*}_{\mathrm{ref\ Adapt}}(n,\,f)\exp[2\pi if\tau]\mathrm{d}f, \tag{20}$$

$$P_{\mathrm{ref\ Adapt}}(n,\,f)=R^{*}_{\mathrm{Comp}}(n,\,f)P_{\mathrm{ref}}(f). \tag{21}$$

By substituting (18) in (21), the adaptive matched filter can be written as

$$P_{\mathrm{ref\ Adapt}}(n,\,f)=\frac{P^{*}_{\mathrm{Rx\,ref}}(f)}{P^{*}_{\mathrm{Tx}}(n,f)}H^{*}_{\mathrm{Tx/Rx}}(f)P_{\mathrm{ref}}(f)=$$

$$=\frac{P^{*}_{\mathrm{Rx\,ref}}(f)P_{\mathrm{ref}}(f)}{|\,P_{\mathrm{Tx}}(n,\,f)\,|^{2}}H^{*}_{\mathrm{Tx/Rx}}(f)P_{\mathrm{Tx}}(n,\,f). \tag{22}$$

Thus, the adaptive range compression is performed by using the actually transmitted pulse $P_{\mathrm{Tx}}(n,\,f)$ (recorded via the 2nd channel of the receiver) instead of a reference LFM pulse, accounting in this way for the actual phase behavior of the transmitted LFM waveform. In addition, the adaptive weighting window

$$w_{\mathrm{ref\ Adapt}}(n,\,f)=\frac{P^{*}_{\mathrm{Rx\,ref}}(f)P_{\mathrm{ref}}(f)}{|\,P_{\mathrm{Tx}}(n,\,f)\,|^{2}} \tag{23}$$

is applied to compensate the distortions of the transmitted LFM pulse envelope. The transfer function $H_{\mathrm{Tx/Rx}}(f)$ just compensates the difference between the measured Tx-pulse and Rx-pulse spectra.

If the major imperfections of the transmitted LFM pulses which change from pulse to pulse are the phase distortions, whereas the pulse envelope is approximately the same (averaged),

$$\left|P_{\mathrm{Tx}}(n,\,f)\right|^{2}\approx\left|P_{\mathrm{Tx\ Av}}(f)\right|^{2}, \tag{24}$$

then the adaptive filtering can be simplified by using the same adaptive window:

$$w_{\mathrm{ref\ Adapt}}(f)\approx\frac{P^{*}_{\mathrm{Rx\,ref}}(f)P_{\mathrm{ref}}(f)}{|\,P_{\mathrm{Tx\ Av}}(f)\,|^{2}}. \tag{25}$$

4. Long-LFM-Pulse Operation Mode with High Duty Cycle

The adaptive range compression filter is matched to each Tx-pulse separately. Therefore, the long-LFM-pulse operation mode has been introduced. Such a mode is designed to guarantee that the consequent Tx-pulses never overlap in the backscattered signals as is shown in Fig. 4. In this section, the parameters of the long-LFM-pulse operation mode are specified.

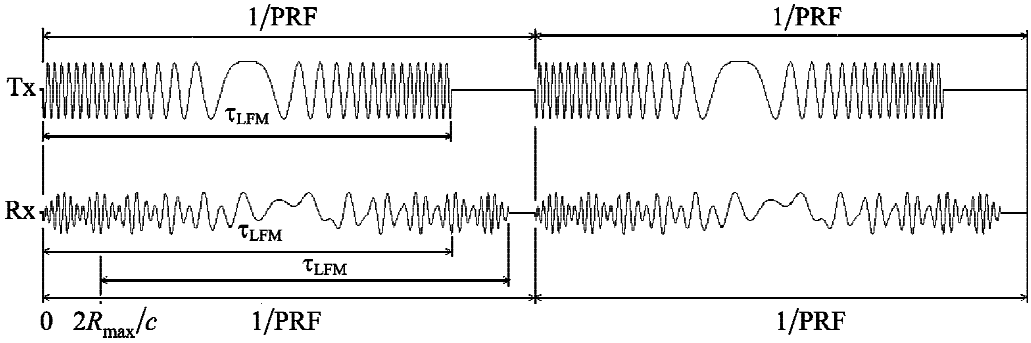

Fig. 4. Long-LFM-pulse (quasi-continuous) operating mode

First, let us consider the Doppler requirements. The pulse repetition frequency PRF has to be high enough to sample unambiguously the highest Doppler frequency in the received signal. If the radar is intended to observe the moving targets of the scene with the maximum radial speed $\pm v_{\max}$, the PRF should satisfy:

$$\frac{\mathrm{PRF}}{2} > \frac{2}{\lambda} v_{\max}. \tag{26}$$

For a still scene, the PRF should be greater than the maximum Doppler frequency from the ground targets, that is

$$\frac{\mathrm{PRF}}{2} > \frac{2}{\lambda} V, \tag{27}$$

where V is the GB-SAR platform (the trolley) speed. The transmitted LFM pulse train with the pulse repetition interval $\mathrm{PRI} = 1/\mathrm{PRF}$ is shown in Fig. 4. Note that in case of working at very close ranges, for example, inside a room, the effect of multiple scattering with the corresponding multiple Doppler frequencies can be observed. In that special case, the selected PRF should be several times higher than the value suggested in (27).

Second, we need to account properly for the time delays of the signals (according to the range to the targets). The operation range of the GB-SAR starts from a few meters from the radar and goes up to a few kilometers. The far range is limited by several factors. The first one is degradation of the cross-range resolution. As it has been discussed above, typically, the GB-SAR resolution is linearly proportional to the range. For example, the aperture length of 3 m gives the resolution (2) of 1 m at a range of 500 m (for $\lambda = 8$ mm). In order to achieve the same resolution of 1 m at a range of 10 km, the required aperture length grows to an unreasonable 60 m. Therefore, the GB-SAR systems typically operate at moderate ranges up to a few kilometers. However, depending on the scene and the radar sensitivity, the signal with the detectable SNR can be observed at ranges up to, for example, $R_{\max} = 20$ km. Therefore, this range should be selected as the maximum unambiguous range. The radar pulse from this range is delayed in time by $2R_{\max}/c$. The total duration of the backscattered pulse from the far target is $2R_{\max}/c + \tau_{\mathrm{LFM}}$ (see Fig. 4).

Finally, the adaptive range compression technique implies that the radar echo received on the n-th PRI is a sum of the backscattered replicas of the n-th Tx-pulse. The overlaying of the consequent Tx-pulses (n and $n+1$) is not allowed since the compression filter is specially adapted to each Tx-pulse separately. It means that the transmission of the next pulse should be started only after the whole response from the previous Tx-pulse is received. Mathematically it reads as

$$\mathrm{PRI} > \frac{2R_{\max}}{c} + \tau_{\mathrm{LFM}}. \tag{28}$$

This relation gives the limitation for the pulse duration,

$$\tau_{\mathrm{LFM}} < \mathrm{PRI} - \frac{2R_{\max}}{c}, \tag{29}$$

assuming that the PRF has already been selected according to (26) or (27). In order to achieve the high sensitivity of the radar, the LFM pulse duration τ_{LFM} should be as long as possible, so that the radar should operate with a high duty cycle in a so-called quasi-continuous mode:

$$\mathrm{Duty\ Cycle} = \frac{\tau_{\mathrm{LFM}}}{\mathrm{PRI}} \le 1 - \frac{2R_{\max}/c}{\mathrm{PRI}}. \tag{30}$$

The calculations made for $\mathrm{PRF} = 2.5$ kHz and $\tau_{\mathrm{LFM}} = 250$ μs give the maximum unambiguous range $R_{\max} = 22.5$ km and the duty cycle of 62.5 % (see Table 1). In some cases the duty cycle can be additionally limited by the transmitter hardware overheating.

5. Range-Doppler Processing of GB-SAR Data

The range-Doppler algorithm is one of the simplest SAR data processing methods [7, 8]. In this section, this algorithm is briefly described in relation to the GB-SAR operating mode. The geometry of the GB-SAR data processing problem is shown in Fig. 5. The trolley with the GB-SAR system is moving on rails along the x axis at a constant velocity V as

$$x_T(t) = Vt, \qquad -T_S/2 \le t \le T_S/2, \qquad L_S = VT_S. \tag{31}$$

Due to the coherent processing of the backscattered radar pulses, the path length L_S is the synthetic aper-

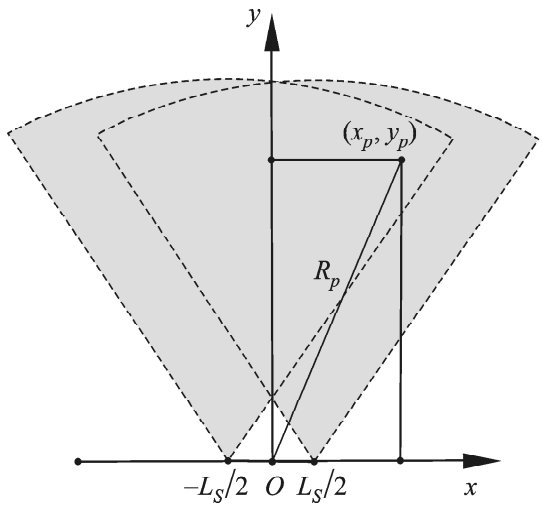

Fig. 5. Geometry of the GB-SAR data processing problem

ture length, and the time of motion T_S is the time of synthesis. The range from the radar to a point target located at the point (x_p, y_p) changes with time as

$$R(x_p, y_p, t) = \sqrt{\left(x_p - x_T(t)\right)^2 + y_p^2} = \sqrt{(x_p - Vt)^2 + y_p^2}. \tag{32}$$

Usually, the synthetic aperture length L_S is much smaller than the range to the target so that the range (32) can be approximately written as

$$R(x_p, y_p, t) \approx R_p - \frac{x_p}{R_p} Vt + \frac{(Vt)^2}{2R_p}\left(1 - \frac{x_p^2}{R_p^2}\right), \tag{33}$$

$$R_p = \sqrt{x_p^2 + y_p^2}.$$

The signal backscattered from the target can be written as

$$\begin{aligned} &s(x_p, y_p, t, \tau) = \\ &= a(x_p, y_p)\, p_{\mathrm{RC}}\left[\tau - \tau_R(x_p, y_p, t)\right] \exp\left[i\varphi(x_p, y_p, t)\right], \\ &\tau_R(x_p, y_p, t) = 2R(x_p, y_p, t)/c, \\ &\varphi(x_p, y_p, t) = -\frac{4\pi}{\lambda} R(x_p, y_p, t). \end{aligned} \tag{34}$$

The signal is delayed according to the range to the target, and the delay changes with the slow time t (from pulse to pulse) meaning that the signal migrates on the range. In our experiments, the aperture length was less than the range resolution so that the range migration effect can be ignored.

The instantaneous Doppler frequency of the signal is given as

$$\begin{aligned} f(x_p, y_p, t) &= \frac{1}{2\pi} \frac{\mathrm{d}\varphi(x_p, y_p, t)}{\mathrm{d}t} \approx \\ &\approx \frac{2}{\lambda} \frac{x_p}{R_p} V - \frac{1}{\lambda} \frac{V^2 t}{R_p}\left(1 - \frac{x_p^2}{R_p^2}\right) = \\ &= F_{\mathrm{DC}}(x_p, R_p) + F_{\mathrm{DR}}(x_p, R_p)t. \end{aligned} \tag{35}$$

The signal behaves as the one with the LFM on the Doppler frequency with the central Doppler frequency $F_{\mathrm{DC}}(x_p, R_p)$ and the Doppler rate $F_{\mathrm{DR}}(x_p, R_p)$.

Two targets situated at the same range but at some different azimuth positions have correspondingly different central Doppler frequencies. It means that the radar image can be obtained simply by applying the FFT in the azimuth direction to the range-compressed data. The image will be obtained in the range-Doppler coordinates (F_p, R_p). One can say that the FFT of the length N_{FFT} forms a fan of N_{FFT} synthetic beams. The obtained image can be resampled from the range-Doppler coordinates (F_p, R_p) to the ground coordinates (x_p, y_p) by using the following relations:

$$x_p = \frac{\lambda F_p}{2V} R_p, \qquad y_p = \sqrt{R_p^2 - x_p^2} = R_p \sqrt{1 - \left(\frac{\lambda F_p}{2V}\right)^2}. \tag{36}$$

The Doppler frequency resolution is determined by the time of synthesis as

$$\rho_F = \frac{K_X}{T_S}. \tag{37}$$

According to (36), the frequency resolution (37) turns into the angular azimuth resolution (2) as

$$\theta_X = \frac{\Delta x}{R} = \frac{\lambda \Delta F}{2V} = K_X \frac{\lambda}{2VT_S} = K_X \frac{\lambda}{2L_S}. \tag{38}$$

Actually, the Doppler rate term $F_{\mathrm{DR}}(x_p, R_p)$ should be compensated before applying the FFT. This operation is called focusing. However, the Doppler rate term can be neglected if the instant Doppler frequen-

cy variations during the time of synthesis do not exceed the frequency resolution cell,

$$\frac{1}{\lambda}\frac{V^2(T_S/K_X)}{R} \le \rho_F, \tag{39}$$

or, in other words, if the quadratic phase variations do not exceed $\pi/2$,

$$\frac{4\pi}{\lambda}\Delta R \le \pi/2. \tag{40}$$

Both conditions pose the same limitation on the aperture length:

$$L_S \le K_X\sqrt{\lambda R}. \tag{41}$$

This simple processing mode is called a non-focused SAR and was used to process data in our experimental GB-SAR system.

6. Autofocusing of GB-SAR Images via Prominent Point Processing

The motion of the trolley platform can be insufficiently steady and uniform depending of its mechanical design and construction. In this case, motion errors should be measured and compensated. The following model for the motion errors has been introduced for our GB-SAR system. The trolley is supposed to be moving along the rails (along the *x* axis in Fig. 5) with the velocity *V* and acceleration *A*. Additionally, small random deviations from this uniformly accelerated motion are introduced both along the rails $x_E(t)$ and across the rails $y_E(t)$. These deviations, in particular, include mechanical vibrations of the trolley. The $x_E(t)$ also accounts for possible positioning errors of the trolley from one GB-SAR scan to another when multiple GB-SAR images of the scene are measured (for example, at different polarization at each scan). It is assumed that the mean values of the random deviations are close to zero. Thus, the trolley motion equations can be written as

$$x_T(t) = Vt + A\left(t^2 - (T_S/2)^2\right)/2 + x_E(t), \tag{42}$$

$$y_T(t) = y_E(t), \qquad -T_S/2 \le t \le T_S/2.$$

The trolley starts its motion at the moment of time $t = -T_S/2$ at the position $x_T(-T_S/2) \approx -VT_S/2$ and finishes the motion at $t = T_S/2$ at the position $x_T(T_S/2) \approx V\,T_S/2$. The total travel path is $L_S \approx VT_S$. Note that the trolley position at the central moment of time $t = 0$ is out of the center of the path $x_T(0) \approx -A(T_S/2)^2/2$ if the acceleration is non-zero. The velocity V is the instant velocity at the central moment of time $t = 0$, and it is also the mean observed velocity for the whole time interval T_S. Consequently, the velocity *V* determines the observed mean Doppler frequency of targets F_p (36).

The motion time T_S is exactly known since the processed radar data counts the known number of backscattered radar pulses. The velocity V and acceleration A are the two parameters to be estimated via autofocusing. The trolley travel path length L_S can also be unknown, for example, if there are no limiters on the rails. In this case, the length L_S becomes the third unknown parameter. For perfect image focusing, the unknown random deviations $x_E(t)$ and $y_E(t)$ should also be estimated.

For autofocusing, we have used the well-known prominent point processing (PPP) technique [7, 8] after its adaptation to peculiarities of the GB-SAR mode. In the PPP autofocus, the motion errors are estimated directly from the phase of the signals backscattered from bright isolated point scatterers identified on the scene. In the developed autofocus method, we efficiently exploit the range dependence of the phase errors observed in the backscattered signals. Recently, the similar idea of utilizing the range dependence of the phase errors have been successfully implemented in the local quadratic map-drift autofocus (LQMDA) developed for the airborne SAR [10–12]. The proposed GB-SAR autofocus method is described below in detail.

The range from the radar to a prominent point with the ground coordinates (x_p, y_p) changes with time as

$$R(x_p, y_p, t) =$$

$$= \left(\left[x_p - Vt - A\left(t^2 - (T_S/2)^2\right)/2 - x_E(t) \right]^2 + \right.$$

$$\left. + \left[y_p - y_E(t) \right]^2 \right)^{1/2}. \tag{43}$$

This range dependence can be simplified under the following assumptions:

1) the range to the prominent point $R_p = \sqrt{x_p^2 + y_p^2}$ is much greater than the range variations due to the platform motion;

2) the random deviations $x_E(t)$ and $y_E(t)$ are small so that only their linear terms should be accounted in the approximation.

Under such assumptions, the range dependence (43) can be written approximately as

$$R(x_p,y_p,t) \approx R_{VA}(x_p,y_p,t) + R_E(x_p,y_p,t), \qquad (44)$$

$$R_{VA}(x_p,y_p,t) = R_p - \frac{x_p}{R_p}Vt + \frac{(Vt)^2}{2R_p}\left(1-\frac{x_p^2}{R_p^2}\right) -$$

$$-\frac{x_p}{R_p}\frac{A(t^2-(T_S/2)^2)}{2}, \qquad (45)$$

$$R_E(x_p,y_p,t) =$$

$$= -\frac{x_E(t)\left[x_p - Vt - A\left(t^2-(T_S/2)^2\right)/2\right] + y_p y_E(t)}{R_p}. \qquad (46)$$

The term $R_{VA}(x_p,y_p,t)$ is related to the uniformly accelerated trolley motion, whereas the term $R_E(x_p,y_p,t)$ represents the contribution of the random motion deviations $x_E(t)$ and $y_E(t)$.

In order to use formulas (44)–(46) for autofocusing we have to know the ground coordinates (x_p, y_p) of the prominent points. Originally, the prominent points are detected on the GB-SAR image built in the Doppler-range coordinates (F_p, R_p). The ground coordinates (x_p, y_p) can be calculated from the Doppler-range coordinates (F_p, R_p) by using (36), however, we have to know the trolley velocity V. If the path length L_S of the trolley is exactly known then the motion velocity can be easily calculated as $V = L_S/T_S$. However, if the length L_S is measured inaccurately, the ground coordinates of the prominent points have to be measured using an independent map of the scene, for example, the Google Map as follows.

Among the prominent points detected in the GB-SAR image we select those points that are associated with the particular objects in the Google Map of the scene. By comparing the ground coordinates of these prominent points measured from the Google Map to their Doppler-range coordinates measured from the GB-SAR image, the path length L_S and velocity V are estimated. After that, the ground coordinates of all other prominent points are calculated. In order to improve accuracy, several GB-SAR scans are made and multiple GB-SAR images formed. The ground coordinates of the prominent points estimated at each scan are averaged. From now, the ground coordinates (x_p, y_p) of the prominent points are assumed to be known.

The PPP autofocusing is performed as follows. The complex GB-SAR image is formed by applying the direct FFT to the range compressed data in the azimuth direction. The prominent points are recognized in the image. Then, each prominent point response is isolated by applying a short azimuth window. The windowing preserves a prominent point response and suppresses signals from other targets located at the same range but at other azimuth positions. By using the inverse FFT, the prominent point signal is transformed back to the time domain. After that, the phase of the prominent point signal is measured, unwrapped and recalculated into the range variations (44) for each prominent point.

At the first stage, the velocity V and acceleration A are to be estimated. The measured range variations of each prominent point $R(x_p,y_p,t)$ are approximated by a parabola

$$R_{VA\mathrm{Est}}(x_p,y_p,t) = A_p t^2 + B_p t + C_p. \qquad (47)$$

The coefficients of the parabola are found by minimizing the mean square error (MSE) ("fitting a parabola"):

$$\mathrm{MSE}(A_p,B_p,C_p) =$$

$$= \frac{1}{N}\sum_{n=0}^{N-1}\left[A_p t_n^2 + B_p t_n + C_p - R_p(x_p,y_p,t_n)\right]^2. \qquad (48)$$

Parabola (47) describes the deterministic component of range dependence (45), while the random component of range dependence (46) that contains deviations $x_E(t)$ and $y_E(t)$ is considered as an additional noise during the parabola fitting. The velocity and acceleration (45) are calculated from the coefficients of the parabola as

$$V_{p\,\mathrm{Est}} = -\frac{B_p}{x_p/R_p}, \qquad (49)$$

$$A_{p\,\mathrm{Est}} = -\frac{2}{x_p/R_p}\left[A_p - \frac{(V_{p\,\mathrm{Est}}t)^2}{2R_p}\left(1-\frac{x_p^2}{R_p^2}\right)\right]. \qquad (50)$$

The ratio x_p/R_p appears in the denominator in (49) and (50). It means that the estimation should be done using the prominent points with non-zero values of x_p/R_p and, respectively, with non-zero Doppler frequencies. The velocity and acceleration are estimated for each prominent point independently and then averaged to improve the accuracy,

$$V_{\text{Est}} = \frac{1}{N_p}\sum_{p=1}^{N_p} V_{p\,\text{Est}},$$

$$A_{\text{Est}} = \frac{1}{N_p}\sum_{p=1}^{N_p} A_{p\,\text{Est}}. \qquad (51)$$

When the velocity and acceleration are estimated we can proceed to the second stage – estimation of random deviations $x_E(t)$ and $y_E(t)$. The random term (46) is calculated by subtracting the estimated deterministic part of the range dependence (47) from the measured range dependence $R_p(x_p, y_p, t)$ (44) for each prominent point. The random deviations $x_E(t)$ and $y_E(t)$ in the dependence (46) can be estimated separately for each moment of time t_n by fitting a line

$$R_{E\text{Est}}(x_p, y_p, t) = x_E(t)X_p(t) + y_E(t)Y_p(t),$$

$$X_p(t) = -\frac{x_p - V_{\text{Est}}t - A_{\text{Est}}\left(t^2 - (T_S/2)^2\right)/2}{R_p},$$

$$Y_p(t) = -\frac{y_p}{R_p},$$

by minimizing the MSE:

$$\text{MSE}\left(x_E(t_n), y_E(t_n)\right) =$$

$$= \frac{1}{N_p}\sum_{p=0}^{N_p-1}\left[x_E(t_n)X_p(t_n) + y_E(t_n)Y_p(t_n) - \right.$$

$$\left. -\left\{R(x_p, y_p, t_n) - R_{VA\text{Est}}(x_p, y_p, t_n)\right\}\right]^2.$$

Let us clarify the difference between the first stage and the second one of the autofocus estimation. At the first stage, the velocity V and the acceleration A are estimated independently for each prominent point, and the parabola fitting (47) is performed in the azimuth direction. At the second one, the deviations $x_E(t)$ and $y_E(t)$ are estimated independently for each moment of time, and the line fitting (51) is performed in the range direction.

The estimated cross-rails deviations $y_E(t)$ are compensated by the phase correction

$$\varphi_E(t_n) = \frac{4\pi}{\lambda} y_E(t_n)$$

applied to each received radar pulse independently. The non-uniform along-rails trolley motion is compensated by the interpolation of the received radar data in the azimuth direction. During the interpolation, the data are resampled from the non-uniform sampling grid $x_T(t_n)$ (42) to the uniform grid (31). The interpolation is range-independent. Finally, the compensated radar data are processed by using the common FFT-based GB-SAR algorithm described in Section 5 resulting in a well-focused GB-SAR image.

7. Experimental Results

The performance of the introduced adaptive range compression technique is illustrated in Figs. 6 and 7. The range-compressed data images (the received power in decibels) are shown in Figs. 6*a* and 6*b*. The range (vertical scale) is from 0 (bottom) to 1500 m (top), and the azimuth time (horizontal scale) covers the interval of 6.4 s. The range-compressed data obtained with the ordinary matched filter with the Hamming window is shown in Fig. 6*a*. One can see the noticeable side lobes in the range direction that come from the very close targets. In the image, not only the useful radar returns at far ranges but even the receiver noise is below the side lobes. The side lobes rise because of amplitude and phase imperfections of the transmitted LFM pulses. The range-compressed data obtained with the proposed adaptive matched filter with the Hamming window and with Tx-pulse envelope compensated to the Hamming envelope is shown in Fig. 6*b*. Due to the adaptive compression, the side lobes are reduced significantly down to about 20 dB with respect to the ordinary compression, as clearly illustrated in Fig. 7. Now one can easily observe the receiver noise and the useful signals at far ranges. The presented results convincingly prove the efficiency of the proposed adaptive range compression technique.

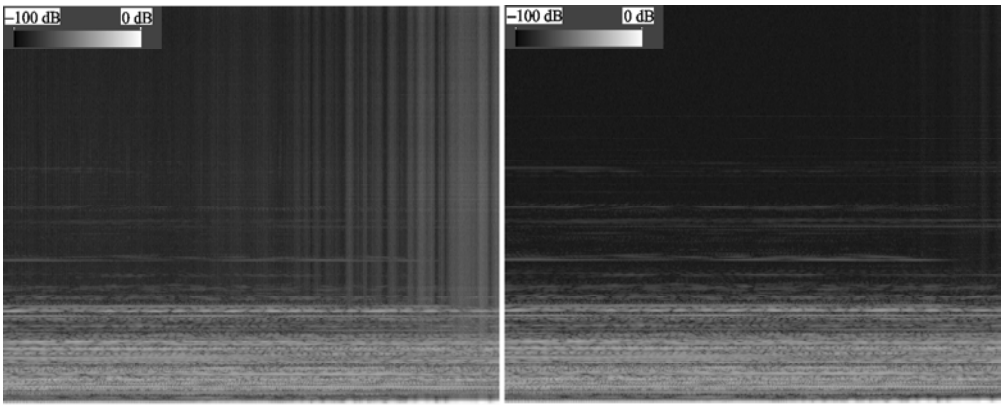

a *b*

Fig. 6. Side lobes observed on range-compressed data: *a* – ordinary matched filter with Hamming window, *b* – adaptive matched filter with Hamming window and Hamming Tx-pulse envelope. The range (vertical scale) is within 0 (bottom) to 1500 m (top); the azimuth time (horizontal scale) is 6.4 s

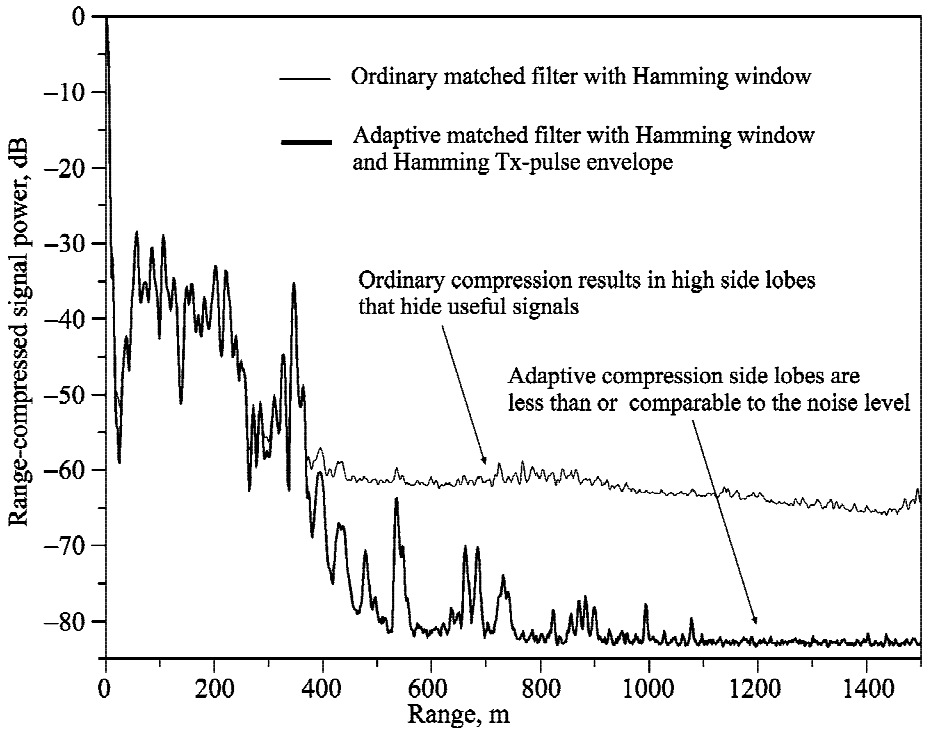

Fig. 7. Range compression side lobes levels achieved with ordinary and adaptive matched filters

In our experiments, the GB-SAR system was operated indoors overviewing the nearby terrain through the open window on the 4th floor of our Institute building. The obtained GB-SAR image along with the Google Map image of the scene are shown in Fig. 8. The scene in the images is about 535 m by 535 m. The bright reflections come from the buildings, in particular, from metallic constructions on the roofs. Reflections from trees are also visible. In the center of the image, one can recognize the radar return from the aircraft Let L-410 Turbolet. Some part of the scene is hidden in radio shadows from the buildings. Note also that visible "azimuth side lobes" are actually poorly focused returns from the targets that were partly illuminated during the observation time (because of shadowing) or from the targets that demonstrate complex scattering being different from scattering from a point target. The

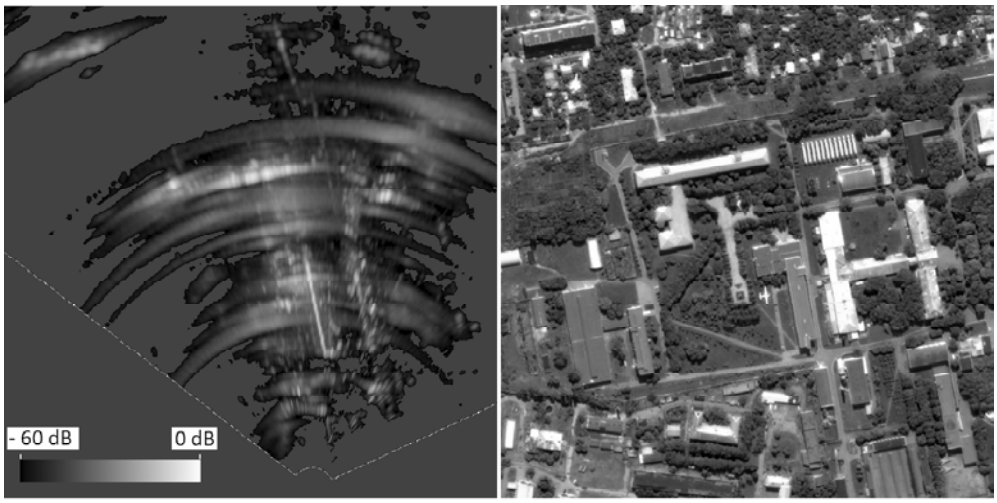

a *b*

Fig. 8. The GB-SAR image (*a*) and the Google Map image (*b*) of the scene (535 m by 535 m)

power decay with the range has been compensated according to the $\sim R^4$ law in Fig. 8*a* (the compensation has not been applied in Figs. 6 and 7). The image demonstrates the scene dynamic range up to 60 dB (the very close target returns were excluded). The obtained results prove the efficiency of the adaptive range compression and confirm the possibility to achieve high azimuth resolution at ranges up to 1.5 km with the ground-based SAR technique at millimeter waves from the imperfectly stabilized platform with autofocusing.

8. Conclusions

An experimental ground-based synthetic aperture radar (GB-SAR) system operating at Ka-band has been successfully created and tested. The implemented high-duty-cycle operating mode (quasi-continuous mode) with the two separate antennas for simultaneous transmission of long LFM pulses and reception of radar returns proves its efficiency and validity. The two-channel receiver used to sample both the transmitted pulses and the backscattered radar echoes allows to realize the highly efficient adaptive pulse compression technique that provides the high dynamic range and low pulse compression side lobes, as well as high pulse-to-pulse coherency and resistance to the phase noise in the transmitted LFM pulses. The described autofocus technique allows obtaining high resolution ground-based SAR images at ranges up to 1.5 km at millimeter waves from the imperfectly stabilized trolley platform.

Acknowledgments

The authors would like to thank all their colleagues at the Department of Microwave Electronics of the Institute of Radio Astronomy for their valuable contributions to this work and for fruitful discussions.

REFERENCES

1. Noferini, L., Pieraccini, M., Mecatti. D., Macaluso, G., Luzi, G., and Atzeni C., 2007. DEM by Ground-Based SAR Interferometry. *IEEE Geosci. Remote Sens. Lett.* 4(4), pp. 659–663.
2. Takahashi, K., Mecatti, D., Dei, D., Matsumoto, M., and Sato, M., 2012. Landslide observation by ground-based SAR interferometry. In: Proceedings of the 2012 IEEE International Geoscience and Remote Sensing Symposium (IGARSS). Munich, Germany, 22-27 July 2012, pp. 6887–6890.
3. Luzi, G., Pieraccini, M., Mecatti D., Noferini, L., Macaluso, G., Tamburini. A., and Atzeni. C., 2007. Monitoring of an Alpine Glacier by Means of Ground-Based SAR Interferometry. *IEEE Geosci. Remote Sens. Lett.* 4(3), pp. 495–499.
4. Martinez-Vazquez, A., and Fortuny-Guasch, J., 2008. A GB-SAR Processor for Snow Avalanche Identification. *IEEE Trans. Geosci. Remote Sens.*, 46(11), pp. 3948–3956.
5. Pipia, L., Fabregas, X., Aguasca, A., and Lopez-Martinez, C., 2013. Polarimetric Temporal Analysis of Urban Environments With a Ground-Based SAR. *IEEE Trans. Geosci. Remote Sens.*, 51(4), pp. 2343–2360.
6. Leva, D., Nico, G., Tarchi, D., Fortuny-Guasch, J., and Sieber, A. J., 2003. Temporal analysis of a landslide by means of a Ground-based SAR interferometer. *IEEE Trans. Geosci. Remote Sens.*, 41(4), pp. 745–752.
7. Carrara, W. G., Goodman, R. S., and Majewski, R. M., 1995. *Spotlight Synthetic Aperture Radar: Signal Processing Algorithms*. Boston, London: Artech House.

8. Cumming, I. G., and Wong, F. H., 2005. *Digital Processing of Synthetic Aperture Radar Data: Algorithms and Implementation*. Norwood, MA: Artech House.
9. Vasilyev, O. Y., Kuzin, A. I., Kravtsov, A. A., Bulakh, E. V., Vinogradov, V. V., and Vavriv, D. M., 2014. Multifunctional Digital Receiver-Spectrometer. *Radiofizika i Radioastronomia*, 19(3), pp. 276–289 (in Russian).
10. Gorovyi, I. M., Bezvesilniy, O. O., and Vavriv, D. M., 2014. A Novel Trajectory Restoration Algorithm for High-Resolution SAR Imaging. In: Proceedings of the 15th International Radar Symposium (IRS 2014). Gdansk, Poland, 16-18 June 2014, pp. 170–173.
11. Vavriv, D. M., Bezvesilniy, O. O., Kozhin, R. V., Vinogradov, V. V., Volkov, V. A., Gorovyi, I. M., and Sekretarov, S. S., 2014. X-Band SAR System for Light-Weight Aircrafts. In: Proceedings of the 15th International Radar Symposium (IRS 2014). Gdansk, Poland, 16-18 June 2014, pp. 501–505.
12. Bezvesilniy, O. O., Gorovyi, I. M., and Vavriv, D. M., 2013. Efficient Estimation of Residual Trajectory Deviations from SAR Data. In: Proceedings of the 10th European Radar Conference (EURAD-2013). Nuremberg, Germany, 9-11 October 2013, pp. 188–191.

А. А. Безвесильный, Д. М. Ваврив, В. А. Волков, А. А. Кравцов, Е. В. Булах, В. В. Виноградов, С. С. Секретарев

Радиоастрономический институт НАН Украины,
ул. Краснознаменная, 4, г. Харьков, 61002, Украина

ЭКСПЕРИМЕНТАЛЬНАЯ НАЗЕМНАЯ РСА-СИСТЕМА Ka-ДИАПАЗОНА

Разработана экспериментальная наземная радиолокационная система с синтезированной апертурой (РСА-система), работающая в Ka-диапазоне длин волн. Система спроектирована для работы с вершины холма или крыши здания и т. п. для построения изображений нижерасположенной местности. В статье описана аппаратная часть радиолокатора, режим работы и оригинальные методы обработки данных. Применен режим работы с длинными импульсами с линейной частотной модуляцией с высокой скважностью (квази-непрерывный режим). Предложена техника сжатия импульсов с эффективным адаптивным согласованным фильтром, которая обеспечивает высокий динамический диапазон и высокую когерентность радиолокационной системы. Для точной оценки и компенсации ошибок движения радиолокационной платформы применен метод автофокусировки по сигналам от ярких точек. Достигнутая эффективность наземной РСА-системы проиллюстрирована на экспериментальных данных.

О. О. Безвесільний, Д. М. Ваврів, В. А. Волков, А. А. Кравцов, Є. В. Булах, В. В. Виноградов, С. С. Секретарьов

Радіоастрономічний інститут НАН України,
вул. Червонопрапорна, 4, м. Харків, 61002, Україна

ЕКСПЕРИМЕНТАЛЬНА НАЗЕМНА РСА-СИСТЕМА Ka-ДІАПАЗОНУ

Розроблено експериментальну наземну радіолокаційну систему з синтезованою апертурою (РСА-систему), яка працює в Ka-діапазоні довжин хвиль. Систему спроектовано для роботи з вершини пагорба або даху будівлі тощо для побудови зображень нижче розташованої місцевості. В статті описано апаратну частину радіолокатора, режим роботи і оригінальні методи обробки даних. Застосовано режим роботи з довгими імпульсами з лінійною частотною модуляцією з високою скважністю (квазі-неперервний режим). Запропоновано техніку стискання імпульсів з ефективним адаптивним узгодженим фільтром, що забезпечує високий динамічний діапазон та високу когерентність радіолокаційної системи. Для точної оцінки і компенсації помилок руху радіолокаційної платформи використано метод автофокусування за сигналами від яскравих точок. Досягнута ефективність наземної РСА-системи проілюстрована на експериментальних даних.

Received 17.04.2015